Broadband FUV imaging spectrometer: advanced design with a single toroidal uniform-line-space grating

Lei Yu,[1,2] Shu-rong Wang,[1,*] Yi Qu,[1] and Guan-yu Lin[1]

[1]Changchun Institute of Optics, Fine Mechanics and Physics, Chinese Academy of Sciences, Changchun, Jilin 130033, China

[2]Graduate School of the Chinese Academy of Sciences, Beijing 100039, China

*Corresponding author: top1gods@mail.ustc.edu.cn

Received 29 April 2011; revised 22 June 2011; accepted 23 June 2011; posted 27 June 2011 (Doc. ID 146520); published 27 July 2011

Performances of a far-ultraviolet (FUV) imaging spectrometer in an advanced design are presented with a toroidal uniform-line-space (TULS) grating. It provides high spatial resolution and spectral resolution for a broadband and a wide field of view. A particular analysis for the grating aberrations, including all the high-order coefficients neglected by previous existing designs, was generated for indicating their significance. The analysis indicates that these high-order off-axis aberrations would have a remarkable influence on the design results. The transcendental equations composed of these aberration coefficients do not have analytic solutions in algebra. To solve the problem, the past designs always do some simplified calculation which only suits a narrow field of view and waveband. Thus, the optimization of the genetic algorithm is introduced to propose reasonable ranges of optical parameters. Then ZEMAX software is used to obtain the final optical system from these ranges. By comparing different design results of the same example, our advanced TULS design performs better than conventional TULS design and spherical varied-line-space grating design, and as well as the toroidal varied-line-space design. It is demonstrated that aberrations are minimized when the TULS design is operated by our method. The advanced design is low-cost, easy to fabricate, and more suitable for FUV observations.

OCIS codes: 120.4570, 120.6200, 300.6190.

1. Introduction

From the radiation of particles through the far-ultraviolet (FUV) waveband distributing in the ionosphere, a wealth of information about the structure and variation of the ionosphere is provided. The imaging spectrometer, which plays an important role in the field, can analyze FUV emission sources spatially and spectrally [1]. The FUV imaging spectrometer, which can supply excellent broadband imaging quality and high spectral resolution, can help us understand the dynamic phenomena and the influence of the ionosphere. At present, many payloads for ionosphere observation have been used, such as the Atmospheric Infrared Sounder, the Special Sensor Ultraviolet Spectrographic Imager, the Global Ultraviolet Imager, the Remote Atmospheric and Ionospheric Detection System, and the Ionospheric Mapping and Geocoronal Experiment [2–5].

The radiation of the emission sources in the ionosphere is very weak. Therefore, the imaging spectrometer for ionosphere observation consists of the fewest optical parts: a telescope with one or two mirrors and a single-grating normal or near-normal incident spectrometer.

Single-grating designs have the highest spectrometer transmission efficiency, an extremely important consideration in the FUV waveband. The present development of single-grating designs makes

0003-6935/11/224468-10$15.00/0

it a subject of discussion of potential interest for observations. Werner [6] gave the basic theory of diffraction gratings with the well known descriptions by Beutler and Namioka [7,8]. Two approaches have been used for correcting aberrations: uniform-line-spaced gratings ruled on a toroidal blank and varied-line-space (VLS) gratings ruled on a spherical blank. The grooving spacing is constant in the former case but follows a polynomial law along the surface in the other case.

The classical toroidal uniform-line-spaced (TULS) grating can eliminate aberrations by using different radii of curvature in the sagittal direction and the meridian direction in special arrangements. For example, Huber and Tondello used TULS grating in the Rowland circle [9]. Cotton *et al.* [10] used it in the Rowland mount in one dimension and the Wadsworth mount in the other dimension. The spherical varied-line-space (SVLS) grating studied by Harada and Kita [11] controls aberrations by adjusting the parameters for ruling variations. The proper distribution of line spacing helps this design perform better than the TULS design. Onaka *et al.* [12] also used the technology and obtained the same performance. Both the classical TULS and SVLS designs have been adopted for FUV observations in laboratory and space applications.

These two methods also admit to some limitations: they are suitable only for a narrow field of view and waveband. Thus, a new logical extension of the concepts composed of TULS design and SVLS design has been suggested to rule VLS on the toroidal surface to produce a toroidal varied-line-space (TVLS) grating. Such a design can improve performance. More detailed researches were completed by Poletto and Thomas [13].

In this paper, we try to improve the classical TULS grating design to obtain the best performance. In previous designs, some high-order off-axis aberration coefficients in three directions have been ignored. These coefficients impact performances seriously when the imaging spectrometer is used in a broadband and a wide field of view. Based on this principle, we obtain aberration-corrected conditions and analyze the influences of the absent high-order aberrations in the other designs. Equations composed of these aberration coefficients are transcendental equations that have no strict analytical solutions. Therefore, we choose the genetic algorithm to calculate these conditions as a whole instead of individually, to get the optimum ranges of parameters satisfying the requests of the imaging spectrometer. Then we use ZEMAX software to simulate the optical system and get the final optimum design. To show the advantages of the advanced design, we use ZEMAX to simulate the classical TULS, SVLS, and TVLS designs for the same example. In comparison with these results, we find that the advanced design performs better than classical TULS and SVLS designs, and as well as the TVLS design. In the last section, we calculate the design spectral resolution of the imaging spectrometer.

2. Description of the Principle and Method of Aberration Correction

A. Basic Equations and Light-Path Function for the Single-Grating Spectrometer

The Cartesian coordinate system of the single-grating spectrometer is shown in Fig. 1. The origin, O, is on the grating vertex. The x axis is normal to the surface at O, the y axis is perpendicular, and the z axis is parallel to the grooves. The direction of the slit length is along the z axis. $A(x,y,z)$, which is any point on the entrance slit, launches light on the point $P(u,w,l)$ of the grating surface. Then the light is diffracted to the point $A'(x',y',z')$. $B(x,y,0)$ and $B'(x',y',0)$ are the projection points of $A(x,y,z)$ and $A'(x',y',z')$ in the XOY plane. i and θ are the incident angle and diffraction angle of the grating that satisfy the grating equation $d(\sin i+\sin\theta)=m\lambda$, where m is the order of diffraction, λ is the wavelength of the light, and d is the width of the groove of the grating.

The expression of the toroidal surface is described as a Taylor series:

$$u=\frac{w^2}{2R}+\frac{l^2}{2\rho}+\frac{w^4}{8R^3}+\frac{l^4}{8\rho^3}+\frac{w^2l^2}{4R^2\rho}+\ldots. \tag{1}$$

By substituting Eq. (1) into the light-path function F, A through P to A', F is expressed as

$$\begin{aligned}F&=<AP>+<A'P>=<AO>+<A'O>-\frac{w}{d}m\lambda\\&=F_{00}+F_{10}+F_{20}+F_{30}+F_{40}+F_{02}+F_{12}\\&\quad+F_{22}+F_{04}++F_{Z0}+F_{Z1}+F_{Z2}+O(w^5)\\&\quad+O(l^5)+O(z^3)+\ldots\end{aligned} \tag{2}$$

R is the radius of curvature in the meridian direction, and ρ is the radius of curvature in the sagittal direction of the toroidal grating, where $O(w^5)$ are terms in w^5 and higher, $O(l^5)$ are terms in l^5 and higher, and $O(z^3)$ are terms in z^3 and higher that can be neglected. F_{ij} stand for different aberrations and are listed in Table 1.

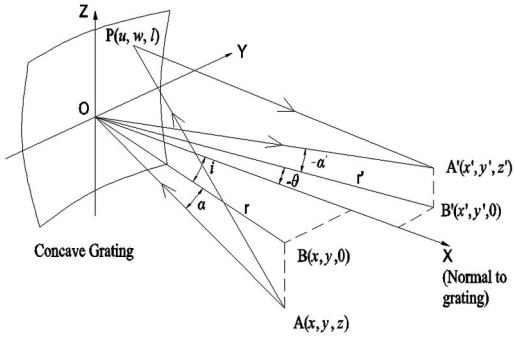

Fig. 1. Schematic diagram of the grating.

Table 1. Terms with Their Associate Aberration

Aberration	Terms
Basic light-path	F_{00} and F_{Z0}
Basic grating equation	F_{10} and F_{Z1}
Spherical aberration	F_{40}, F_{22} and F_{04}
Astigmatism	F_{02} and F_{Z2}
Spectral focus	F_{20}
Coma	F_{30} and F_{12}

B. Aberration Coefficients Analysis

The terms in Table 1 are expressed as follows:

$$\begin{cases} F_{00} = r + r' \\ F_{Z0} = \frac{1}{2}\left(\frac{z^2}{r} + \frac{z'^2}{r'}\right) \end{cases}, \tag{3}$$

$$\begin{cases} F_{10} = w\left(\frac{m\lambda}{d} - \sin i - \sin\theta\right) \\ F_{Z1} = \frac{w}{2}\left(\frac{z^2 \sin i}{r^2} + \frac{z'^2 \sin\theta}{r'^2}\right) - l\left(\frac{z}{r} + \frac{z'}{r'}\right) \end{cases}, \tag{4}$$

$$\begin{cases} F_{40} = \frac{w^4}{8}\left[\frac{4\sin^2 i}{r^2}\left(\frac{\cos^2 i}{r} - \frac{\cos i}{R}\right) - \frac{1}{r}\left(\frac{\cos^2 i}{r} - \frac{\cos i}{R}\right)^2 + \frac{1}{R^2}\left(\frac{1}{r} - \frac{\cos i}{R}\right)\right. \\ \left. + \frac{4\sin^2\theta}{r'^2}\left(\frac{\cos^2\theta}{r'} - \frac{\cos\theta}{R}\right) - \frac{1}{r'}\left(\frac{\cos^2\theta}{r'} - \frac{\cos\theta}{R}\right)^2 + \frac{1}{R^2}\left(\frac{1}{r'} - \frac{\cos\theta}{R}\right)\right] \\ F_{22} = \frac{w^2 l^2}{4}\left[\frac{2\sin^2 i}{r^2}\left(\frac{1}{r} - \frac{\cos i}{\rho}\right) - \frac{1}{r}\left(\frac{\cos^2 i}{r} - \frac{\cos i}{R}\right)\left(\frac{1}{r} - \frac{\cos i}{\rho}\right) + \frac{1}{R\rho}\left(\frac{1}{r} - \frac{\cos i}{R}\right)\right. \\ \left. + \frac{2\sin^2\theta}{r'^2}\left(\frac{1}{r'} - \frac{\cos\theta}{\rho}\right) - \frac{1}{r'}\left(\frac{\cos^2\theta}{r'} - \frac{\cos\theta}{R}\right)\left(\frac{1}{r'} - \frac{\cos\theta}{\rho}\right) + \frac{1}{R\rho}\left(\frac{1}{r'} - \frac{\cos\theta}{R}\right)\right] \\ F_{04} = \frac{l^4}{8}\left[\frac{1}{\rho^2}\left(\frac{1}{r} - \frac{\cos i}{\rho}\right) - \frac{1}{r}\left(\frac{1}{r} - \frac{\cos i}{\rho}\right)^2 + \frac{1}{\rho^2}\left(\frac{1}{r'} - \frac{\cos\theta}{\rho}\right) - \frac{1}{r'}\left(\frac{1}{r'} - \frac{\cos\theta}{\rho}\right)^2\right] \end{cases}, \tag{5}$$

$$\begin{cases} F_{30} = \frac{w^3}{2}\left[\frac{\sin i}{r}\left(\frac{\cos^2 i}{r} - \frac{\cos i}{R}\right) + \frac{\sin\theta}{r'}\left(\frac{\cos^2\theta}{r'} - \frac{\cos\theta}{R}\right)\right] \\ F_{12} = \frac{wl^2}{2}\left[\frac{\sin i}{r}\left(\frac{1}{r} - \frac{\cos i}{\rho}\right) + \frac{\sin\theta}{r'}\left(\frac{1}{r'} - \frac{\cos\theta}{\rho}\right)\right] \end{cases}, \tag{6}$$

$$\begin{cases} F_{02} = \frac{l^2}{2}\left(\frac{1}{r} - \frac{\cos i}{\rho} + \frac{1}{r'} - \frac{\cos\theta}{\rho}\right) \\ F_{Z2} = \frac{w^2}{2}\left(\frac{z^2 \sin^2 i}{r^3} + \frac{z'^2 \sin^2\theta}{r'^3}\right) - wl\left(\frac{z\sin i}{r^2} + \frac{z'\sin\theta}{r'^2}\right) - \frac{l^2}{4}\left(\frac{z^2}{r^3} + \frac{z'^2}{r'^3}\right) \\ -\frac{z^2}{8}\left[2w^2\left(\frac{\cos^2 i}{r^3} - \frac{\cos i}{Rr^2}\right) + l^2\left(\frac{4}{r^3} - \frac{2\cos i}{\rho r^2}\right)\right] - \frac{z'^2}{8}\left[2w^2\left(\frac{\cos^2\theta}{r'^3} - \frac{\cos\theta}{Rr'^2}\right) + l^2\left(\frac{4}{r'^3} - \frac{2\cos\theta}{\rho r'^2}\right)\right] \\ F_{20} = \frac{w^2}{2}\left(\frac{\cos^2 i}{r} - \frac{\cos i}{R} + \frac{\cos^2\theta}{r'} - \frac{\cos\theta}{R}\right) \end{cases}. \tag{7}$$

Some high-order terms in Eqs. (5)–(7) are neglected in different designs. Here we will discuss these terms with the help of Fig. 2. Figure 2 gives the relationships of the aberration coefficients with the off-axis amount (changes of w, l, and z). We assume that values of parameters in Eqs. (5)–(7) have been given where $\lambda = 120\,\text{nm}$, $d = 1/600\,\text{mm}$, $i = 5°$, $r = 145\,\text{mm}$, $r' = 155\,\text{mm}$, $R = 150\,\text{mm}$, and $\rho = 145\,\text{mm}$. These values are not optimum and are only used to clearly show the relationship between aberration coefficients and the off-axis amount. It is convenient for us to study influences of the higher-order off-axis aberrations.

F_{40} was the only considered high-order coefficient that previous designs had in common. The change of F_{40} with w and l is shown in Fig. 2(e). Here we compare the other high-order coefficients with F_{40}. In Figs. 2(b)–2(d), when w and l increase to certain values, F_{04} is approximately equal to F_{40}, F_{22} and F_{12} increase even more rapidly than F_{40}. Figure 2(a) gives the relationship between F_{Z2} and w and l. The coefficient $z*$ included in the vertical ordinates indicates that changes of $z*$ are proportional to z. The value of coordinate z is an important factor for the locations of the slit and the detector. It should have a reasonable value to guarantee that there is no interference between the slit and the detector. If z is large enough, the influence of F_{Z2} will be more serious than that of F_{40}. The analysis illustrates that the high-order coefficients F_{04}, F_{22}, F_{12}, and F_{Z2} should be considered in the design, when the field

Equations (5)–(7) denote on- and off-axis aberrations. When these equations are set to zero, a stigmatic spectrometer, which is to realize the coincidence of the meridian and the sagittal focal curves over the waveband and the field of view of interest, will be obtained as the optimum structure. It is hard to apply such a perfect coincidence. The optimization is to make the design approach the ideal situation as closely as possible.

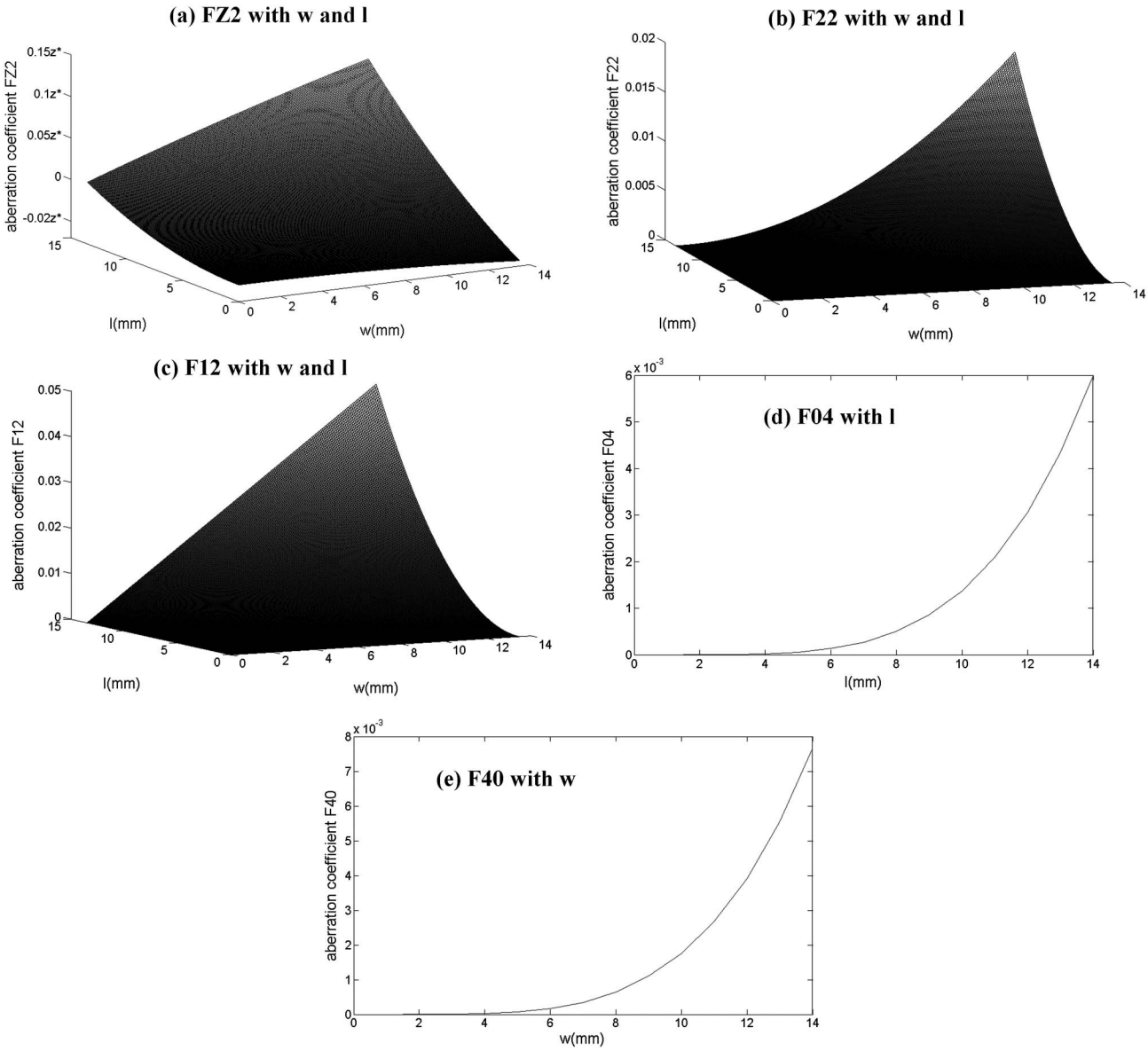

Fig. 2. Relationships between different aberration coefficients F_{Z2}, F_{22}, F_{12}, F_{04}, F_{40}, and w and l.

of view and the waveband in observation are wide (it equals the large values of w, l, and z). Here we will discuss which coefficients were neglected in existing designs.

1. Although Haber in 1950 [14] had analyzed all the aberration coefficients for the TULS design, F_{Z2} is still ignored and F_{22}, F_{04}, and F_{12} are simplified to some extent in later designs to facilitate the calculation in the application. When the field of view and the waveband of interest required are narrow, it is reasonable. Once the off-axis amount increases a great deal, the method for adjusting the parameters of the grating to decrease off-axis aberrations will result in the shifting of the stigmatic wavelengths out of the waveband under observation.

2. In the SVLS design, the light source and its diffraction image point are located on a line $x = R$ to make F_{22}, F_{04}, F_{12}, and F_{02} zero, but F_{Z2} is also ignored. The additional parameters for ruling variations improve the ability of correcting off-axis aberrations in SVLS design. But in the absence of adding the different radius, the incident angle has to be small to reduce astigmatism. The missing F_{Z2} and the invariability of the radius limit the field of view and the waveband under observation. If the incident angle is requested to be larger, the performance of SVLS design both on- and off-axis will degrade.

3. TVLS design considers F_{Z2} but neglects the other high order terms: F_{22}, F_{04}, and F_{12}. The advantages of additional parameters for ruling variations and different radius in two directions decrease the effects of missing coefficients. It makes the sagittal focal curve intersect the meridian focal curve in a waveband to guarantee on-axis and off-axis performance of the design. There are two problems with

the TVLS design. One is that the fabrication technique of the grating is complicated, and the error of the grating may influence the final performance of the design. The other is that it barely maintains the same performances in a very wide waveband or a wide field of view with a flat focal plane.

In our design, we try to consider all the aberration coefficients discussed above to improve the performances of the TULS design. All these steps make it possible to enlarge the field of view and the spectral region of the design in application.

C. Aberration Elimination Method and Problem Formulation

It is apparent that Eqs. (5)–(7) are transcendental equations that have no analytical solutions in the strict meaning of algebra. It determines that reasonable optical parameters cannot be calculated by algebraic calculation. For a narrow field of view and waveband, there is no need to consider those high-order aberration coefficients discussed in Subsection 2.B for the conventional TULS, SVLS, and TVLS designs. Therefore, the optimizations of these designs simplified some conditions (e.g., two arms of the spectral imaging system were usually calculated before the optimization by special locations such as the Rowland circle) to make the other optical parameters calculable in algebra. This method will introduce serious influences of the off-axis amount to the design for a wide field of view and waveband. In such a situation, small changes of the single-grating system will also exercise considerable influence on the performance of the spectrometer. These reasons make the initial reasonable optical structure difficult to obtain. As we all know, if we start the optimization with software such as ZEMAX or CODEV directly, without reasonable initial optical parameters, the process will be complicated and produce abnormal parameters that cause the final optimization to fail. Because of the lack of design guidelines and reasonable initial optical parameters, the optimization will be difficult and lengthy. It requires that an appropriate method be applied to calculate the reasonable ranges of initial optical parameters.

To achieve this goal, we need to consider computer-aided optimization that can minimize each variable of F in total rather than as individuals. The genetic algorithm (GA) was first proposed by Holland [15] and extended further by DeJong and Goldberg [16,17]. It is an efficient search technique, which supplies the rules of natural genetics in a given search space. GA mimics the process of natural selection and starts with artificial individuals. It attempts to produce descendants that are better than their parents in terms of a certain quantitative measure. The GA is being applied successfully to find solutions to problems in engineering and science, especially as a general problem-solving technique in many optimization problems. It is well suited to problems with complex, discontinuous, and discrete functions. By the use of the GA, Eqs. (5)–(7) can be solved without any omission in the application of wide field of view and broadband. In addition, reasonable parameters can be obtained conveniently and rapidly.

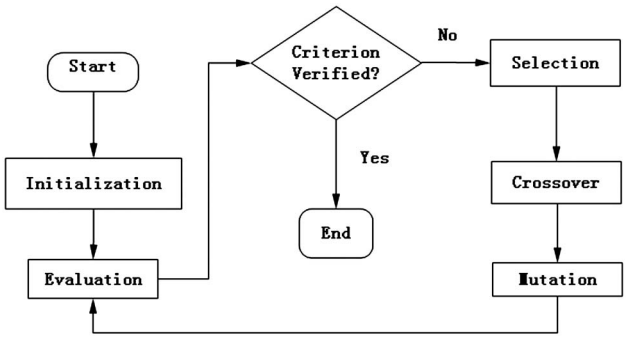

Fig. 3. Genetic algorithm flowchart.

Rather than starting from a single-point solution within the search space, as in traditional methods, the genetic algorithm starts with an initial set of solutions. Figure 3 presents the GA flow chart. An initial population of individuals is generated at first. Each individual is evaluated in terms of a certain "fitness function" that can guide the algorithm to the desired region of the search space. Then three genetic operations (selection, crossover, and mutation) are carried out. First, the selection assures that individuals are copied to the next generation with a probability associated with their fitness values. However, it does not search the space further, because it just copies the previous candidate individuals. Second, the crossover allows the new generation to inherit properties from old ones. Third, mutation is a random perturbation to one or more genes during the evolutionary process. The purpose of the mutation operator is to avoid local optima and premature convergence. The searching process terminates when the predefined criterion is satisfied.

The most important purpose for our design is to have a minimum of total aberrations. For this aim, the objective function W is formulated as

$$\text{Minimize } W = \sum_{i=1,j=2} F_{ij}, \tag{8}$$

where F_{ij} is the aberration term in Eqs. (5)–(7).

The GA cannot be directly applied to the problem with its constraints. In order to solve the problem, the form of the objective function must be modified to be independent of constraints. For this aim, a penalty function calculating the value of the violation of constraints is determined. By using this penalty function, the objective function is modified to a form that includes constraints. The objective function is called a penalized objective function. Here are the constraints:

$g_1 = \rho - R \le 0$, $g_2 = R\cos i\cos\alpha - r \le 0$, $g_3 = r - R/\cos i\cos\alpha \le 0$, $g_4 = R\cos i\cos\alpha' - r' \le 0$, $g_5 = r' - R/\cos i\cos\alpha' \le 0$.

Then the penalty function is given as

$$C = \sum_{i=1}^{m} c_i, \tag{9}$$

where m is the number of constraints, c_i is the value of each constraint. c_i can be calculated as

$$\text{if } g_i \geq 0 \text{ then } c_i = g_i, \tag{10}$$

$$\text{if } g_i < 0 \text{ then } c_i = 0. \tag{11}$$

The penalized objective function can be formulated as

$$\Phi = W[1 + P \cdot C], \tag{12}$$

where Φ is the penalized objective function, P is a constant which is a variable for each problem. To determine the fitness of each individual, a criterion must be specified to make selection in the population. The criteria used in the study is given as

$$D_i = (\Phi_{\max} + \Phi_{\min}) - \Phi_i, \tag{13}$$

where D_i is the fitness value of each individual. In order to determine if an individual is copied to the next generation or not, the fitness factor is used. It can be calculated as

$$D_c = \frac{D_i}{\sum (D_i/n)}, \tag{14}$$

where n is the number of individuals in the population.

We make the design vector $x = (\rho, r, r', i, \theta)$. The lower limits of the design vector consists of the initial population. The crossover probability is chosen as 0.4, and the mutation probability is 0.1. When the total amount of aberrations calculated by the algorithm is smaller than the size of the detector pixel, the termination criterion is satisfied. Then the optimum parameters of the optical structure ranges are obtained.

3. Design and Performance of the Imaging Spectrometer

A. Telescope Design and Performance

The general layout of the design imaging spectrometer is shown in Fig. 4. By the requirements of the scientific application, the main parameters of the spectrometer are in Table 2.

Here we use ZEMAX to simulate the telescope. The parameters are in Table 3. The slit is on the focal plane of the telescope. The modulation transfer function (MTF) (Fig. 5) of the telescope is larger than 0.63 at the frequency 20 lp/mm. All the surfaces of the mirrors should be coated aluminum and magnesium fluoride to increase the reflectivity in the far-UV waveband [18].

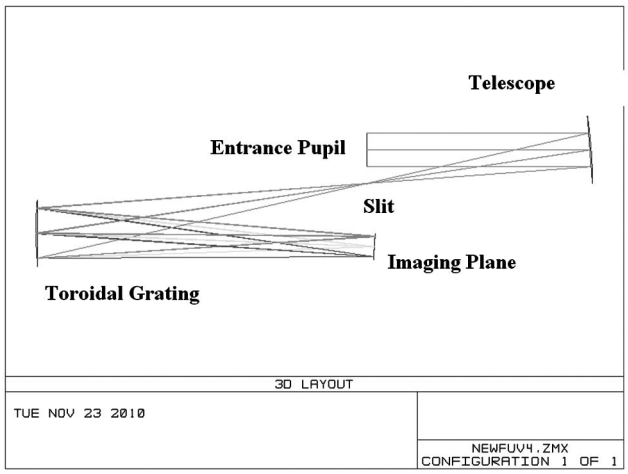

Fig. 4. Layout of imaging spectrometer optical system.

B. Spectral Imaging System Design

Based on the requirements of the volume of the instrument and the resolution, the meridian radius of the toroidal grating is chosen as 150 mm at the beginning of the spectral imaging system design. According to the analysis of Section 2.C, the genetic algorithm starts the optimization with the initial population:

$$145\,\text{mm} < \rho < 155\,\text{mm}, \qquad 3° < i < 8°,$$

$$148\,\text{mm} < L_{S-G} = r/\cos\alpha < 152\,\text{mm},$$

$$148\,\text{mm} < L_{G-I} = r'/\cos\alpha' < 152\,\text{mm},$$

where L_{S-G} is the distance between the slit and the grating, and L_{G-I} is the distance between the grating and the imaging plane. We program the genetic algorithm in C++. After 135 iterations, the termination is satisfied. The process of the convergence history of the aberrations is shown in Fig. 6. The optimum ranges of parameters in Table 4 were obtained when the convergence ended.

Table 2. Parameters of Imaging Spectrometer

Spectral Range	120 nm–180 nm
Spatial resolution/mrad	<1
Spectral resolution/nm	<1 (first order)
Instrument IFOV/(°)	4 × 0.06
Pixel size/μm	25 × 25

Table 3. Parameters of Telescope

Characteristic	Value
Entrance aperture	16 mm
Off-axis distance	15 mm
Focal length	100 mm

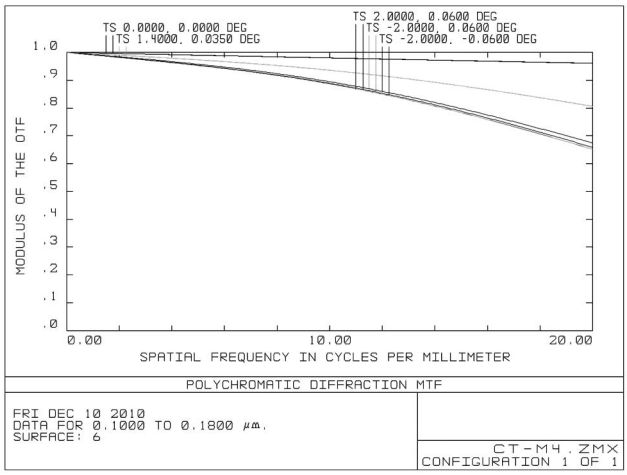

Fig. 5. MTF of telescope.

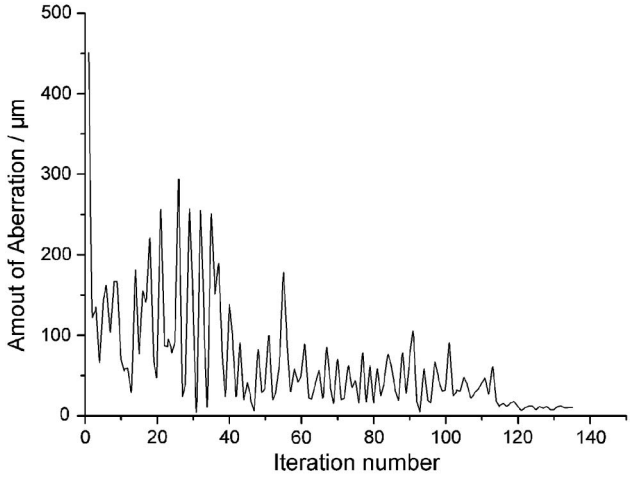

Fig. 6. Convergence history of aberrations.

The design software ZEMAX is used to obtain the final optimum parameters from the optimum ranges generated by the algorithm. These parameters are listed in Table 5.

Table 4. Optimum Ranges of Parameters by Genetic Algorithm

Parameters	ρ/mm	L_{S-G}/mm	L_{G-I}/mm	i/°
Value	[149.40, 149.63]	[148.26, 148.45]	[151, 151.47]	[4.79, 5.43]

Table 5. Parameters of Optical Structure

Characteristic	Optimum Value
Distance L_{S-G}	148.3219 mm
Ruling	600 lp/mm
Curvature R, ρ	150 mm, 149.52 mm
Incident angle	5°
Distance L_{G-I}	151.2280 mm

spot radii versus wavelengths), ray-traced and obtained by ZEMAX, are all shown in Fig. 7. The focal planes of all the designs are flat.

1. Figure 7(a) gives the RMS spot radii, which are smaller than 8 μm in our present design. It shows that excellent imaging quality is obtained over the whole waveband.
2. Figure 7(b) gives the design result of the classic TULS. In the conventional TULS, the parameters of the optical system are calculated by the following formulas:

$$\begin{cases} \cos^2 i/L_{S-G} + \cos^2\theta/L_{G-I} - \cos i/R = 0 \\ 1/L_{S-G} + 1/L_{G-I} - \cos i/\rho - \cos\theta/\rho = 0 \\ \rho = R\cos i\cos\theta \end{cases}. \quad (15)$$

The distance L_{S-G} is 149.5 mm, and the distance L_{G-I} is 149.7 mm. R is 150 mm, and ρ is 149.17 mm. The incident angle is 4.37°. Because of the neglect of the astigmatism F_{Z2} and the simplified calculation of high order spherical aberration and coma, excellent results happen only in the center of the waveband.

3. The result of SVLS design (rms spot radii versus wavelengths) is shown in Fig. 7(c). The calculation can be carried out by the following formulas:

$$\begin{cases} L_{S-G}\cos\alpha = R = L_{G-I}\cos\beta \\ b_2 = \frac{\sigma_0 R}{2m\lambda}\left[\frac{\cos i}{R} - \frac{\cos^2 i}{L_{S-G}} + \frac{\cos\theta}{R} - \frac{\cos^2\theta}{L_{G-I}}\right] \\ b_3 = \frac{\sigma_0 R}{2m\lambda}\left[\frac{\sin i}{L_{S-G}}\left(\frac{\cos i}{R} - \frac{\cos^2 i}{L_{S-G}}\right) + \frac{\sin\theta}{L_{G-I}}\left(\frac{\cos\theta}{R} - \frac{\cos^2\theta}{L_{G-I}}\right)\right] \\ b_4 = \frac{\sigma_0 R^3}{8m\lambda}\left[\frac{4\sin^2 i}{L_{S-G}^2}\left(\frac{\cos i}{R} - \frac{\cos^2 i}{L_{S-G}}\right) + \frac{1}{L_{S-G}}\left(\frac{\cos i}{R} - \frac{\cos^2 i}{L_{S-G}}\right)^2 + \frac{1}{R^2}\left(\frac{\cos i}{R} - \frac{1}{L_{S-G}}\right)\right. \\ \left. + \frac{4\sin^2\theta}{L_{G-I}^2}\left(\frac{\cos\theta}{R} - \frac{\cos^2\theta}{L_{G-I}}\right) + \frac{1}{L_{G-I}}\left(\frac{\cos\theta}{R} - \frac{\cos^2\theta}{L_{G-I}}\right)^2 + \frac{1}{R^2}\left(\frac{\cos\theta}{R} - \frac{1}{L_{G-I}}\right)\right] \end{cases}. \quad (16)$$

C. Performance of the Design

In order to conduct a comparison of our design, different design methods were used to optimize the same example. These methods include conventional TULS, SVLS, and TVLS. The design results (rms

The distance L_{S-G} is 150.72 mm and the distance L_{G-I} is 150.01 mm. R is 150 mm. the incident angle is 5.62°. b_2 is 0.055, b_3 is 0.00487 and b_4 is 0.00052. With the help of the ruling parameters b_i, the imaging quality is better than the conventional TULS design. But for the absence of different radii

and astigmatism coefficient F_{Z2}, it is still worse than TVLS design [Fig. 7(d)] and our advanced design.

4. The advanced TULS design performs equivalent to the TVLS design [in Fig. 7(d)]. In TVLS design, the calculation is as follows:

The distance L_{S-G} is 150.5 mm, and the distance L_{G-I} is 150.05 mm. R is 150 mm, and ρ is 150.23 mm. The incident angle is 4.7°. σ_1 is 0.52667, σ_2 is 0.00253, and σ_3 is 0.000258. Although TVLS design neglects high-order aberration coefficients F_{22}, F_{04}, and F_{12},

$$\begin{cases} L_{S-G}\cos\alpha = R = L_{G-I}\cos\beta \\ \rho = L_{S-G}(\cos i + \cos\theta)\frac{M}{1+M} \\ \sigma_1 = \frac{1}{m}\frac{K_2(\cos i+\cos\theta)-K_1(\cos i+\cos\theta)}{\lambda_1(\cos i+\cos\theta)-\lambda_2(\cos i+\cos\theta)} \\ \sigma_2 = -\frac{3}{2m\lambda}\left[\frac{\sin i\cos i}{L_{S-G}}\left(\frac{\cos i}{L_{S-G}}-\frac{1}{R}\right)+\frac{\sin\theta\cos\theta}{L_{S-G}}\left(\frac{\cos\theta}{L_{S-G}}-\frac{1}{R}\right)\right] \\ \sigma_3 = -\frac{1}{2m\lambda}\left[\frac{4\sin^2 i\cos i}{L_{S-G}^2}\left(\frac{\cos i}{L_{S-G}}-\frac{1}{R}\right)-\frac{\cos^2 i}{L_{S-G}}\left(\frac{\cos i}{L_{S-G}}-\frac{1}{R}-\right)^2+\frac{1}{R^2}\left(\frac{1}{L_{S-G}}-\frac{\cos i}{R}\right)\right. \\ \left.+\frac{4\sin^2\theta\cos\theta}{L_{G-I}^2}\left(\frac{\cos\theta}{L_{G-I}}-\frac{1}{R}\right)-\frac{\cos^2\theta}{L_{G-I}}\left(\frac{\cos\theta}{L_{G-I}}-\frac{1}{R}\right)^2+\frac{1}{R^2}\left(\frac{1}{L_{G-I}}-\frac{\cos\theta}{R}\right)\right] \end{cases}. \quad (17)$$

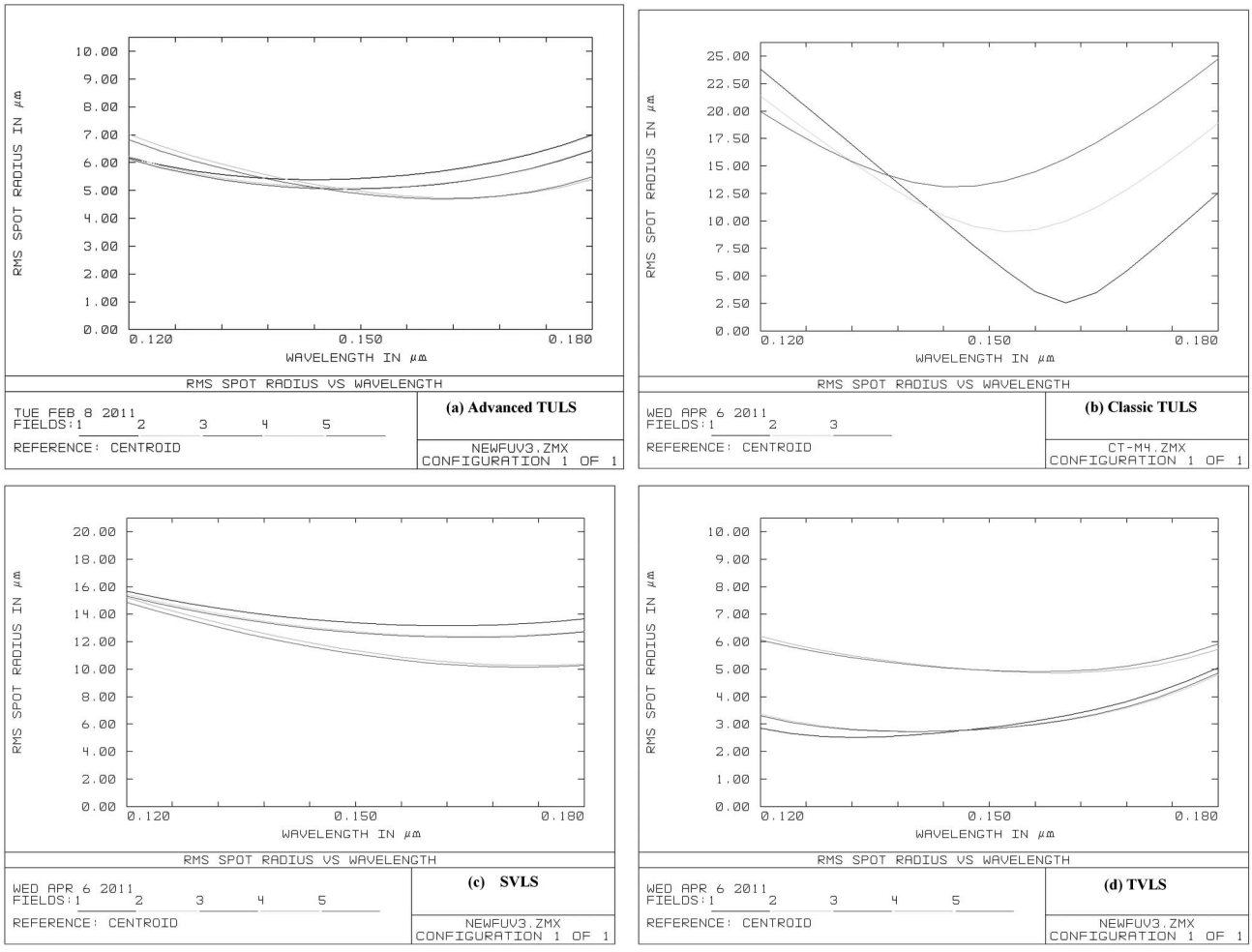

Fig. 7. RMS spots radii versus wavelength of different designs.

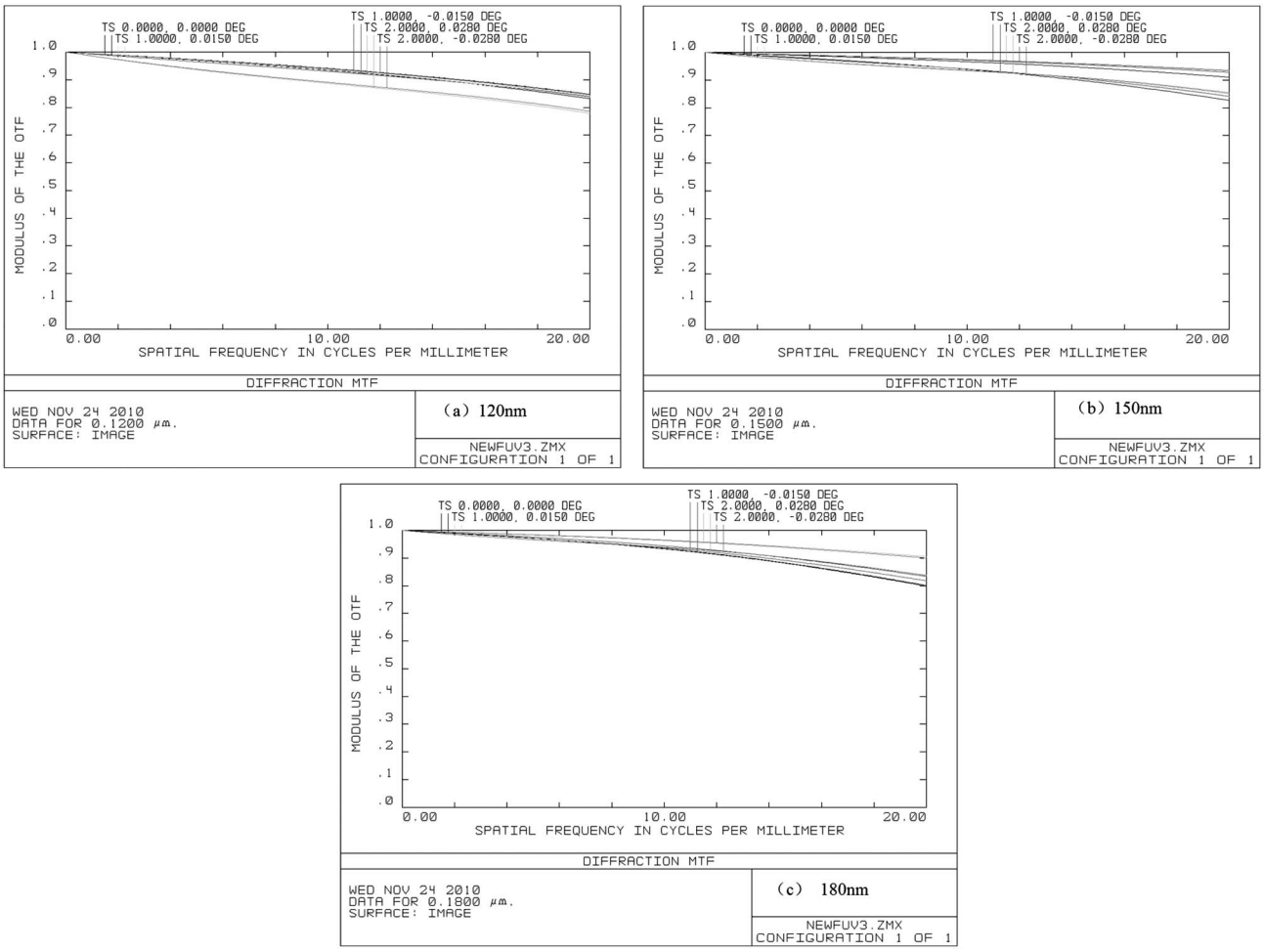

Fig. 8. MTF of the design system under central and marginal wavelengths.

it also provides excellent imaging quality. However, it still reflects the problem of not using coefficients in Fig. 7(d) that the central field of view performs better than the marginal field of view (rms spot radii versus wavelengths in a different field of view have big differences). When the field of view and the waveband increase further, the choice of the flat focal plane will make the phenomenon more prominent and will limit the performance of TVLS design.

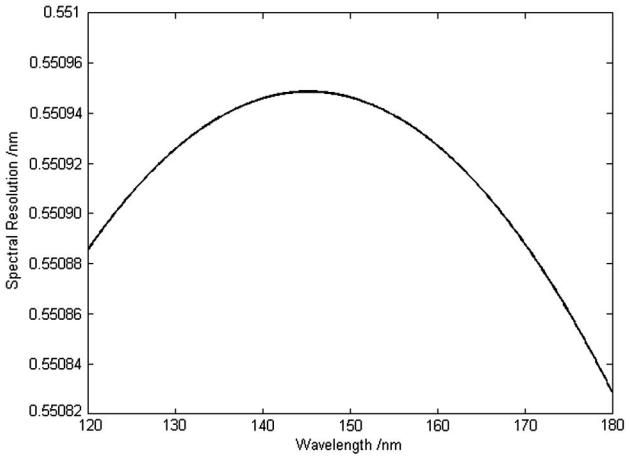

Fig. 9. Relation curve of detector's spectral resolution and wavelength.

The MTF curves of the advanced design are like the functions of spatial frequency in Fig. 8. The MTF of each field of view in the central and marginal wavelengths is larger than 0.75 at the Nyquist frequency for the detector. All the results prove that the advanced TULS design performs excellently. The method is convenient and lower in cost than the TVLS design.

D. Analysis of Spectral Resolution

Here we will calculate the precise spectral resolution of the design. The detector controls limit spectral resolution, which is decided by the pixel size and parameters of the imaging spectrometer. It is also the minimum spectral resolution that can be owned by the imaging spectrometer. The spectral resolution can be expressed as

$$\Delta\lambda_D = \frac{2db}{mL_{G-I}}\cos\theta\cos\sigma, \tag{18}$$

where b is the size of the detector pixel, which is $25\,\mu$m and $L_{G-I} = 151.23$ mm. The corresponding curve of $\Delta\lambda_D$ with the wavelength is shown in Fig. 9.

The width of the slit and the grating decide the spectral resolution of the optical system. The spectral resolution can be expressed as

$$\Delta\lambda_S = \frac{sd}{mL_{S-G}}\cos i\cos\alpha, \tag{19}$$

where the width of the slit $s = 0.05\,\text{mm}$, $d = 1/600\,\text{mm}$, $i = 5°$, $\alpha = 1°$, and $L_{S-G} = 148.3\,\text{mm}$. Therefore, $\Delta\lambda_S = 0.56\,\text{nm}$.

For the imaging spectrometer, the half-width of the spectral resolution introduced by aberrations along the slit should also be considered [19]. Only when the change is less than the spectral resolution of the system is the design available. The largest half-width of the spectral change appears at the end of the slit. The spectral resolution can be expressed as

$$\Delta\lambda_{A\,\max} = \frac{dc}{8mR^2}\cos i\cos\theta|2W\sin(i-\theta) - c\cos i(\sin i + \sin\theta)|, \tag{20}$$

where W is 27 mm in our design and c is the length of the slit. R is the radius of the grating in the meridian direction, which is 150 mm. Then we can calculate that $\Delta\lambda_{A\,\max} = 0.35\,\text{nm}$, which is smaller than $\Delta\lambda_D$ and $\Delta\lambda_S$. In fact, when the radius of the disc of the confusion introduced by aberrations is smaller than 1/3 of the width of the slit, the influence of the aberration for the spectral resolution can also be neglected.

The relationship of $\Delta\lambda_D$ and $\Delta\lambda_S$ can be shown as follows: when $\Delta\lambda_D$ is bigger than $\Delta\lambda_S$, the designed spectral resolution is $\Delta\lambda_D$. When $\Delta\lambda_D$ is smaller than $\Delta\lambda_S$, the designed spectral resolution is $\Delta\lambda_S$. Therefore, the designed spectral resolution of the imaging spectrometer is $\Delta\lambda_S$, which is 0.56 nm.

The process of the calculation can also be used at the beginning of the design to estimate the initial values of basic optical parameters.

4. Conclusion

An advanced aberration-corrected TULS grating imaging spectrometer was designed for ionosphere observation. In the present design, we studied aberrations in three dimensions and obtained more comprehensive corrected conditions for TULS design. The analysis of aberration coefficients indicated that high-order terms had important influences when the amount of off-axis increases. To obtain reasonable solutions of the transcendental equations in the composition of all the aberration coefficients, the GA was introduced. With the help of the GA and ZEMAX software, the final optimization of the advanced TULS design was obtained. It was effective in reducing aberrations in a spectral broadband and an extended field of view for a flat focal plane. The design results show that the advanced design has high spatial resolution and spectral resolution. The instrument design concept and theory can be adapted to other wavebands and across larger fields in a wide range of applications.

The research was supported by the National Natural Science Foundation of China (NSFC) under grant 41074126.

References

1. F. W. Schenkel, B. S. Ogorzalek, J. C. Larrabee, F. J. Leblanc, and R. E. Huffman, "Ultraviolet daytime auroral and ionospheric imaging," Appl. Opt. **24**, 3395–3405 (1985).
2. R. P. McCoy, K. F. Dymond, G. G. Fritz, S. E. Thonnard, R. R. Meier, and P. A. Regeon, "Special sensor ultraviolet limb imager: an ionospheric and neutral density profiler for the Defense Meteorological Satellite Program satellites," Opt. Eng. **33**, 423–429 (1994).
3. L. J. Paxton, A. B. Christensen, D. Morrison, B. Wolven, H. Kil, Y. Zhang, B. S. Ogorzalek, D. C. Humm, J. O. Goldsten, R. DeMajistre, and C.-I. Meng, "GUVI: a hyperspectral imager for geospace," Proc. SPIE **5660**, 228–239 (2004).
4. S. Habraken, C. Jamar, P. Rochus, S. B. Mende, and M. Lampton, "Optical design of the FUV spectrographic imager for the IMAGE Mission," Proc. SPIE **3114**, 544–553 (1997).
5. D. Morrison, L. Paxton, D. Humm, B. Wolven, H. Kil, Y. Zhang, B. S. Ogorzalek, and C.-I. Meng, "On-orbit calibration of the special sensor ultraviolet scanning imager (SSUSI)—a far-UV imaging spectrograph on DMSP F16," Proc. SPIE **4485**, 328–337 (2002).
6. W. Werner, "Geometric optical aberration theory of diffraction gratings," Appl. Opt. **6**, 1691–1699 (1967).
7. H. G. Beutler, "Theory of the concave grating," J. Opt. Soc. Am. **35**, 311–350 (1945).
8. T. Namioka, "Theory of the concave grating. I," J. Opt. Soc. Am. **49**, 446–460 (1959).
9. M. C. E. Huber and G. Tondello, "Stigmatic performance of an EUV spectrograph with a single toroidal grating," Appl. Opt. **18**, 3948–3953 (1979).
10. D. M. Cotton, T. Cook, and S. Chakrabarti, "Single-element imaging spectrograph," Appl. Opt. **33**, 1958–1962 (1994).
11. T. Harada and T. Kita, "Mechanically ruled aberration-corrected concave gratings," Appl. Opt. **19**, 3987–3993 (1980).
12. T. Onaka, T. Miyata, H. Kataza, and Y. Okamoto, "Design for an aberration-corrected concave grating for a mid-infrared long-slit spectrometer," Appl. Opt. **39**, 1474–1479 (2000).
13. L. Poletto and R. J. Thomas, "Stigmatic spectrometers for extended sources: design with toroidal varied-line-space gratings," Appl. Opt. **43**, 2029–2038 (2004).
14. H. Haber, "Torus grating," J. Opt. Soc. Am. **40**, 153–165 (1950).
15. J. H. Holland, *Adaptation in Natural and Artificial Systems* (University of Michigan Press, 1975).
16. K. De Jong, "The analysis and behavior of class of genetic adaptive systems," Ph. D. dissertation, University of Michigan (1975).
17. D. E. Goldberg, *Genetic algorithms in search, optimization, and machine learning reading* (Addison-Wesley, 1989).
18. W. R. Hunter, J. F. Osantowski, and G. Hass, "Reflectance of aluminum overcoated with MgF2 and LiF in the wavelength region from 1600 to 300 at various angles of incidence," Appl. Opt. **10**, 540–544 (1971).
19. T. Onaka, "Aberration-corrected concave grating for the mid-infrared spectrometer aboard the Infrared Telescope in Space," Appl. Opt. **34**, 659–666 (1995).